ACS ENGINEERING Au
AN OPEN ACCESS JOURNAL OF THE AMERICAN CHEMICAL SOCIETY

Open Access
This article is licensed under CC-BY 4.0

pubs.acs.org/engineeringau
Article

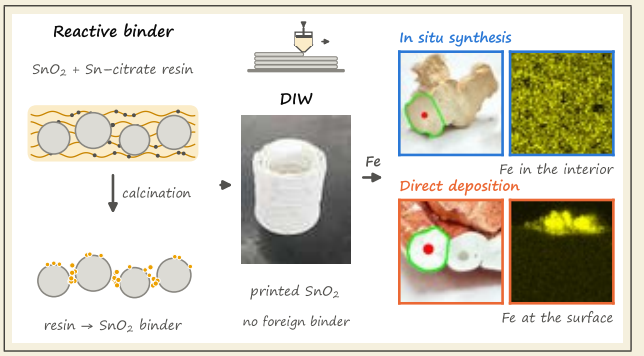
Reactive-Binder Direct Ink Writing of Structured SnO_2 Catalyst Supports with Volumetric Incorporation of Fe

Carolina Mendes Furlan Ferreira, Anderson Luis Barbosa, Cátia Alexandra Podence Alves, Andre Luiz da Silva, Douglas Gouvêa, and Bruno Ramos*

Cite This: https://doi.org/10.1021/acsengineeringau.6c00022
Read Online

ACCESS | Metrics & More | Article Recommendations | Supporting Information

ABSTRACT: Tin oxide (SnO_2) is a chemically stable, redox-active metal oxide widely employed as a catalyst support in heterogeneous reactions, gas sensing, and energy-related applications. Here, we present a reactive-binder strategy for the additive manufacturing of structured SnO_2 catalyst supports via direct ink writing (DIW) using a Pechini-derived polymeric complex that acts simultaneously as a rheological modifier and an oxide precursor. This dual role eliminates the need for inert thickeners or foreign oxide binders while contributing to the final solid loading after calcination. The resulting paste exhibits suitable viscoelastic properties for extrusion-based shaping and enables the fabrication of self-supporting structures that retain their geometric integrity after calcination. The printed bodies exhibit an interconnected pore architecture (54.8% mercury-accessible porosity; median intrusion diameter of approximately 138 nm), suitable for precursor infiltration and catalytic functionalization. Coating experiments with Fe-containing species show that, within the examined filament cross-sections, in situ synthesis promotes comparatively homogeneous incorporation, whereas direct deposition results in surface-localized agglomerates. Discrete Si-rich inclusions, most probably introduced during paste preparation, were also identified, indicating that contamination control during processing is required in addition to the binder chemistry. These results show that reactive-binder DIW provides a route for producing structured SnO_2 supports accessible to the volumetric incorporation of Fe-containing species, with potential applicability to other single- and mixed-oxide systems relevant to structured catalytic reactors and energy-transition technologies.



KEYWORDS: *Tin oxide, direct ink writing, reactive binder, structured catalyst supports, Fe-containing species, porous ceramics*

1. INTRODUCTION

The energy transition is possibly one of the biggest challenges that we face as a society in the 21st century. Driven by extreme climate events attributed to rising atmospheric CO_2 levels, promoted by the extensive use of oil- and coal-derived combustion, this new transition pushes us to find alternative energy systems and routes to produce materials essential for our modern society. Overcoming this challenge requires a collective and multidisciplinary effort, of which the design of robust, efficient and sustainable catalysts is a major example.

Recent work from our group has explored the synthesis and application of metal oxides in processes relevant to the energy transition, including the conversion of CO_2 to value-added fuels,[1] and the synthesis of ammonia from dissolved N_2 under ambient conditions,[2] where they act as catalysts. In earlier development stages, the catalysts are typically synthesized in powder form, but for achieving higher technology readiness levels and facilitating scale-up, having them in easily handled forms is essential. In practical large-scale applications, solid catalysts are typically shaped into or fixed onto larger particles, such as pellets or other geometrical fillings, which are then inserted into reaction vessels. These pieces of equipment are intended to promote optimal contact between the reactants, usually fluids, and the catalysts; the geometry of the support is designed to facilitate this process while also controlling the pressure drop through the equipment, reducing the energy demand. To fix the catalysts onto supporting materials, synthesis methods such as ultrasonic spray,[3] jet-inking,[4] spin-coating,[5] or dip-coating[6] can be used. While these methods are well established, tailoring the support properties and geometry remains an active research area.

Among the various catalyst supports reported in the literature, ceramic materials are frequently employed due to

Received: April 3, 2026
Revised: October 23, 2026
Accepted: October 26, 2026

ACS Publications
© XXXX The Authors. Published by American Chemical Society

Downloaded from pubs.acs.org/aeacb3/article-pdf/doi/10.1021/acsengineeringau.6c00022/6911515151/acsengineeringau.6c00022.pdf by CTR UNIV DA FEI user on 09 November 2026

their high thermal and chemical stability, mechanical robustness, and resistance to sintering under harsh reaction conditions. In addition, their surface chemistry can be tuned to optimize catalyst−support interactions, enhancing the dispersion, stability, and activity of the active phase. The specialized literature has shown that the nature of the support affects catalyst performance, so tailoring its composition—particularly avoiding unwanted species, especially metallic ions—is a key aspect of materials processing. Studies report that supports with high surface area and tailored porosity, such as mesoporous metal oxides, promote uniform dispersion, stabilize nanoparticle size (often below 6 nm), and generate active metal−support interfaces that boost turnover frequencies by orders of magnitude in reactions such as carbon monoxide oxidation.[7] In addition, supports that provide oxygen vacancies, specific redox states, and controlled surface chemistry (for example, cerium dioxide and titanium dioxide) enhance oxygen activation and strengthen metal−support bonding. These features can improve reaction rates as well as selectivity and durability in a range of industrial processes, including electrocatalysis, preferential oxidation, and steam reforming.[8]

Several routes have been developed to produce ceramic catalyst supports with tailored composition, morphology, and surface chemistry. Advanced additive manufacturing techniques, such as extrusion-based 3D printing (direct ink writing, DIW) and stereolithography, allow the direct fabrication of structured supports with customized geometries, optimized flow channels, and hierarchical porosity.[9] These methods facilitate the incorporation of specific design parameters from the early stages of fabrication.

Conventional ceramic processing relies heavily on polymeric binders to impart plasticity, cohesion, and shape retention during forming. These additives, however, are transient and must be removed prior to densification, often through thermal debinding, a step that can introduce defects such as cracking, carbon retention, or anisotropic shrinkage if not carefully controlled.[10] Such challenges underscore the limitations of inert binders, which serve only as processing aids and contribute no functional role to the final ceramic body. In contrast, reactive binders offer a transformative alternative: they simultaneously tailor rheology during shaping and convert into the target oxide upon calcination, thus eliminating foreign binder-derived species and contributing to the final solid loading.[11] Recent developments have demonstrated their potential to reduce binder-derived foreign species in ceramic components while simplifying debinding and improving microstructural integrity.[12,13] Building on this approach, we previously reported a method for preparing TiO_{22} structures by direct ink writing without the use of inorganic binders, thereby avoiding incorporation of unwanted metal cations,[12] and here we extend this methodology to SnO_2, a material valued for its thermal and chemical stability, tunable electronic structure, strong metal−support interactions, and morphological flexibility. These properties make SnO_2 particularly attractive as a support for metals in electrocatalytic processes,[14] especially under oxidizing or high-temperature conditions, NO_x reduction,[15] and biocatalysis,[16] among others.

2. METHODOLOGY

2.1. Materials

Tin(IV) oxide (SnO_2, Balestro Inc.) was used as the primary ceramic phase. Tin oxalate (SnC_2O_4, ≥98%, Sigma-Aldrich) was employed as the inorganic precursor in the preparation of the Pechini-type polymeric resin. Citric acid (≥99.5%, Synth), monoethylene glycol (≥99.0%, Neon), nitric acid (65%, Synth), and deionized water were used for preparing the resin. Iron(III) nitrate nonahydrate ($Fe(NO_3)_3{\cdot}9H_2O$, 99%, Labsynth) was used as the iron precursor for the in situ coating. All reagents were used without further purification.

2.2. Formulation of the Ceramic Paste

The extrudable SnO_2 ceramic paste was prepared by mixing in a glass beaker using a mechanical overhead stirrer (Model 715, Fisatom, Brazil) at 1500 rpm a polymeric resin with dried SnO_2 powder, which was gradually incorporated to achieve the desired solid loading, followed by mixing at 2500 rpm for 60 s to ensure homogeneity. The compositions were adjusted to contain 76.02, 74.37, 75.00, and 72.50 wt % commercial powder, designated RB-76.0, RB-74.4, RB-75.0, and RB-72.5, respectively (Table 1). The RB prefix denotes the use of the reactive binder, while the numerical suffix reports the commercial SnO_2 fraction in the wet paste.

Table 1. Ceramic Paste Formulation Nomenclature and Nominal Composition[a]

Formulation	Commercial powder	Wet resin	Resin water	Resin oxide residue	Total nominal oxide
RB-76.0	76.02	23.98	9.06	1.86	77.88
RB-74.4	74.37	25.63	9.69	1.99	76.36
RB-75.0	75.00	25.00	9.45	1.94	76.94
RB-72.5	72.50	27.50	10.40	2.13	74.63

[a]All entries are wt % of the wet paste. Water and resin-derived SnO_2 residues were calculated using the measured resin values of 37.8 and 7.75 wt %, respectively; total nominal oxide is commercial powder plus resin-derived residue.

The polymeric resin, containing a precursor for in situ formation of SnO_2 nanoparticles, was prepared via a modified Pechini process.[17] Briefly, monoethylene glycol was heated to approximately 70 °C together with citric acid, using a magnetic stirrer. Once a homogeneous mixture was obtained, i.e., a clear, transparent solution, the sample was kept for 30 min in the polymerization process at 120 °C. Meanwhile, the tin oxalate solution was stirred with 23 wt % diluted nitric acid for about 1 h to obtain the Sn(IV) precursor needed to form SnO_2 during calcination. Finally, the tin oxalate was slowly added to the monoethylene glycol and citric acid mixture at 120 °C while being stirred at a constant speed for 30 min. Calcination of the resin at 900 °C for 5 h in air left 7.75 g of SnO_2 residue per 100 g of resin; this value is a calcination residue and not a process yield. The resin water content was determined by gravimetry as 37.8 ± 2.2 wt % after drying samples at 120 °C for 48 h.

2.3. Direct Ink Writing

The pastes were printed using a Cartesian-type 3D printer (DuraPrinter C02, Duracer) equipped with a piston-driven reservoir feeding an auger extrusion system. Printing was carried out at a reservoir pressure of 3 bar through a 1.2 mm nozzle. Slicing was performed in Ultimaker Cura with the following parameters: layer height = 0.8 mm; initial layer height = 0.5 mm; line width = 1.2 mm; flow = 200%; printing speed = 15 mm s^{-1}; travel speed = 30 mm s^{-1}; spiralized outer contour mode = on. No top/bottom layers were printed to obtain hollow-walled geometries. The printed test geometry was a 40 × 40 mm hollow cylinder, designed to evaluate the shape fidelity and self-support capability of the paste. After printing, samples were dried under ambient conditions for 48 h and calcined in air at 500 °C (2 °C min^{-1}) for 5 h.

Downloaded from pubs.acs.org/aeach3/article-pdf/doi/10.1021/acsengineeringau.6c00022/6911515151/acsengineeringau.6c00022.pdf by CTR UNIV DA FEI user on 09 November 2026

https://doi.org/10.1021/acsengineeringau.6c00022
ACS Eng. Au XXXX, XXX, XXX−XXX

2.4. Catalyst Coating

To evaluate the applicability of the material as a catalytic support, coating experiments were performed using Fe-containing species deposited onto fragments of the same 3D-printed SnO_2 piece, in line with previous studies by the group on the use of iron oxides in emerging photocatalytic processes.[2] Two distinct preparation routes were investigated: (i) direct deposition and (ii) in situ synthesis.

For samples prepared by direct deposition (DD), the substrate was immersed in an aqueous suspension of previously synthesized nanoparticulate iron oxide, which had been subjected to 10 min of ultrasonication to reduce particle agglomeration. Three immersion steps were performed; between each step, the coated substrate was dried at 120 °C for 30 min to promote adhesion of the deposited material and evaporation of the solvent. After the final drying stage, the samples were calcined at 450 °C for 12 h to ensure solvent removal and thermal treatment of the deposited species.

Samples prepared by in situ synthesis (ISS) involved immersion of the substrates in a diluted polymeric resin containing iron precursors. The precursor resin was prepared using the polymeric precursor (Pechini) method, similarly to the reactive binder formulation. The synthesis employed anhydrous citric acid (45.8 wt %) as the complexing agent, monoethylene glycol (30.5 wt %) as the polymerizing agent, and iron(III) nitrate nonahydrate (23.6 wt %) as the iron source. Initially, citric acid was dissolved under stirring and moderate heating. Iron nitrate was then added to the solution, promoting complexation of Fe^{3+} ions by the carboxyl groups of citric acid. Subsequently, monoethylene glycol was incorporated into the system, enabling polyesterification between hydroxyl groups of monoethylene glycol and carboxyl groups of the metal citrate, forming a homogeneous polymeric matrix with molecularly dispersed metal ions. The resulting resin was diluted in water (1:4) to lower its viscosity and facilitate penetration into the pores of the printed material. Calcination left 1.92 ± 0.01 g of iron-containing residue, expressed as Fe_2O_3 equivalent, per 100 g of resin. As in the previous procedure, the substrates were immersed and dried three consecutive times; after the final stage, the samples were calcined at 450 °C for 12 h to remove the organic phase and form Fe-containing species.

2.5. Analyses

X-ray diffraction (XRD) patterns were obtained using an X'Pert-MPD (Philips) diffractometer with Cu Kα radiation, operated at 45 kV and 40 mA. The step size was set at 0.02° 2θ per second over the 10−90° 2θ range. Crystallite sizes and lattice parameters were calculated by Rietveld analysis using X'Pert HighScore software with $MgAl_2O_4$ as the standard. The as-received commercial SnO_2 powder was additionally analyzed by XRD and by X-ray fluorescence spectroscopy (XRF). XRF was performed on a pressed powder specimen using an STD-1 standardless calibration for elements from F to U in a Malvern Panalytical Zetium spectrometer. The reported concentrations were normalized to 100%, and the XRF quantification limit was 0.01 wt %. Loss on ignition was measured after heating at 1020 °C for 2 h. The complete XRF composition is provided in Table S1 in the Supporting Information. The powder density was measured using a Micromeritics AccuPyc II 1340 He gas pycnometer after 200 purges for degassing. The specific surface area was determined by nitrogen gas adsorption at 77 K (Micromeritics Gemini III 2375), according to the Brunauer−Emmett−Teller (BET) method. The samples were degassed at 250 °C for approximately 12 h before the experiment using a VacPrep 061 (Micromeritics). Diffuse reflectance infrared Fourier transform (DRIFT) spectroscopy was performed using a Nicolet iS50 spectrometer to identify the functional groups adsorbed on the powder. DRIFT spectra were recorded in the range 400−4000 cm^{-1}.

The rheological behavior was measured using a HAAKE MARS 60 rheometer (Thermo Fisher Scientific) with 35 mm parallel plates and a 1 mm gap at 23 °C, following a preshear at 5 s^{-1} for 30 s and a shear-rate sweep from 1 to 30 s^{-1} and back to 1 s^{-1} to obtain flow curves and hysteresis loops. The apparent viscosity was defined as the viscosity measured at the maximum applied shear rate (30 s^{-1}), providing a consistent basis for comparing the different paste formulations under conditions representative of extrusion flow. Because the rotational flow curve was acquired over the shear-rate range of 1−30 s^{-1}, the true yield stress could not be directly determined. Therefore, an apparent yield stress was operationally defined as the shear stress measured at the penultimate point of the descending branch of the flow cycle, corresponding to the lowest stable shear rate before completion of the test. This criterion minimizes the influence of end-of-test fluctuations while providing a reproducible parameter for comparing the formulations. The hysteresis loop area was calculated numerically using the trapezoidal rule by integrating shear stress (τ) as a function of shear rate ($\dot{\gamma}$) between consecutive experimental points:

$$A = \sum_i \frac{\tau_i + \tau_{i-1}}{2}(\dot{\gamma}_i - \dot{\gamma}_{i-1}) \quad (1)$$

where A is the algebraic hysteresis area, τ is the shear stress, and $\dot{\gamma}$ is the shear rate. The total hysteresis area corresponds to the algebraic sum of the areas of all trapezoids formed between consecutive experimental points. Positive values correspond to clockwise hysteresis loops, whereas negative values indicate counterclockwise hysteresis loops.

Mercury intrusion porosimetry (MIP) measurements were carried out using an AutoPore IV porosimeter (Micromeritics Inc.), in accordance with ISO 15901-1:2005, to determine the distribution of mercury-accessible pore-throat diameters and the mercury-accessible porosity of the printed supports. Scanning electron microscopy (SEM) and energy-dispersive X-ray spectroscopy (EDS) analyses were performed using an environmental scanning electron microscope (ESEM) Quanta 650 FEG (FEI Inc.), equipped with Quantax EDS microanalysis systems (Bruker Inc.). Measurements were conducted under high-vacuum conditions using secondary-electron (SE) and backscattered-electron (BSE) imaging with the Everhart−Thornley (ETD) and backscattered-electron (BSED) detectors, respectively. Surface regions, fracture zones, and polished cross-sections were examined. In all cases, the samples were carbon-coated prior to analysis. For polished cross-sections, the samples were embedded in a transparent epoxy resin suitable for ceramographic preparation of porous materials, ensuring effective infiltration and preservation of the microstructure. After resin curing, the mounted specimens were subjected to grinding and polishing using a Tegramin-30 system (Struers Inc.). The average particle size was determined by digital SEM image analysis using automated segmentation in Python.[18] Micrographs were first converted to grayscale and processed by automatic thresholding using the Otsu method to separate particles from the background. Morphological operations were then applied to remove noise and separate weakly connected particles, followed by watershed segmentation based on the distance transform to individualize agglomerates.[19] Identified particles were labeled and their projected areas calculated; the equivalent circular diameter was obtained from the area of each particle using image calibration.

3. RESULTS AND DISCUSSION

3.1. Preparation of the Tin Oxide Resin

The resin was prepared as reported in Section 2.2. The resulting material was a viscous, translucent yellowish liquid. Upon calcination, a white powder was obtained, with a calcination residue of 7.75 g of SnO_2 per 100 g of resin. This powder was investigated by XRD, as shown in Figure 1A. Broad diffraction peaks characteristic of nanosized crystallites are observed. Cassiterite (JCPDS card no. 41-1445) was the only phase identified. The commercial SnO_2 powder used to prepare the paste was also analyzed (Figure 1B); its diffraction pattern likewise showed cassiterite, with no crystalline Si-containing phase detected.

The average crystallite size and lattice parameters of the resin-derived nanopowders were calculated after Rietveld refinement of the XRD data. The estimated crystallite size was 10.71 nm, while the refined lattice parameters were $a = b =$

Downloaded from pubs.acs.org/aeach3/article-pdf/doi/10.1021/acsengineeringau.6c00022/6911515151/acsengineeringau.6c00022.pdf by CTR UNIV DA FEI user on 09 November 2026

https://doi.org/10.1021/acsengineeringau.6c00022
ACS Eng. Au XXXX, XXX, XXX−XXX

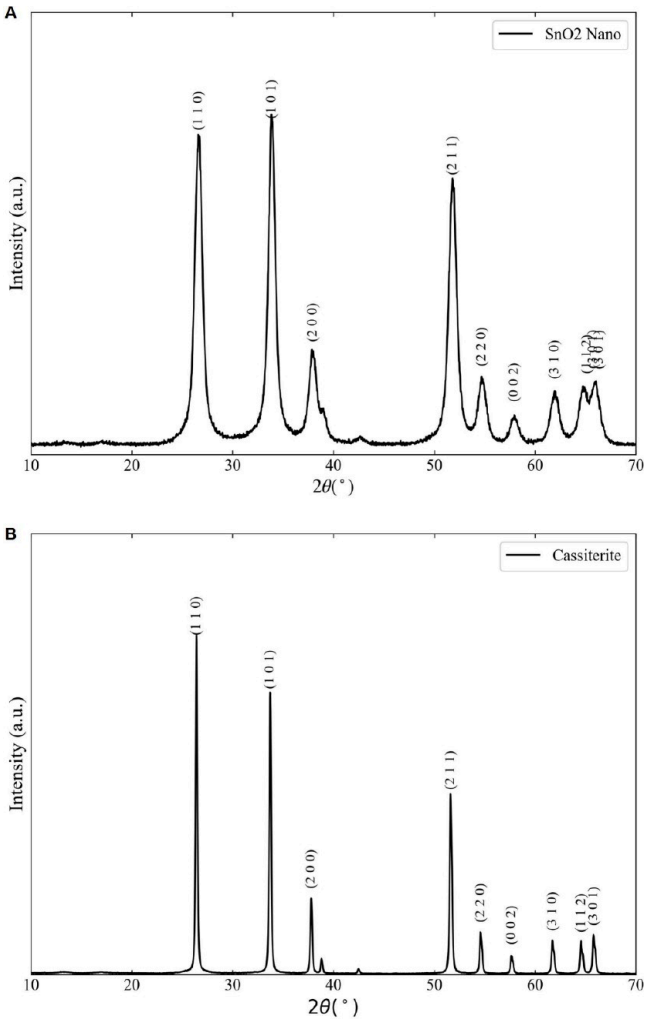


Figure 1. XRD patterns of (A) SnO_2 nanopowder obtained upon calcination of the reactive resin and (B) the commercial SnO_2 powder used to prepare the paste.

4.7355 Å and c = 3.1835 Å. These values are in good agreement with previously reported data,[20,21] and the nanoscale crystallite size is consistent with the broader reflections of the resin-derived powder relative to the commercial starting powder. The patterns also differ in their relative peak intensities: the (101) reflection is the most intense for the resin-derived nanopowder, whereas the (110) reflection dominates the commercial powder. Because the peak positions remain consistent with cassiterite, this change in the (110)/(101) intensity ratio suggests different preferred crystallographic orientations, potentially arising from differences in crystallite morphology or specimen packing. The resin-derived nanopowder exhibited a BET surface area of 47.2 ± 0.1 $m^2\ g^{-1}$, consistent with literature values for SnO_2 nanopowders, and a density of 6.02 ± 0.03 g cm^{-3}, lower than that of bulk SnO_2 (6.91−6.95 g cm^{-3}),[20] due to the nanoscale dimensions and porosity of the powders. XRF analysis of the as-received commercial powder gave 97.9 wt % SnO_2, 1.15 wt % Nb_2O_5, 0.38 wt % PbO, and 0.07 wt % SiO_2; the complete normalized composition is reported in Table S1. These values characterize only the starting powder, not the formulated paste or the printed and calcined body. The DRIFT spectrum of the prepared SnO_2 is given in Figure 2.

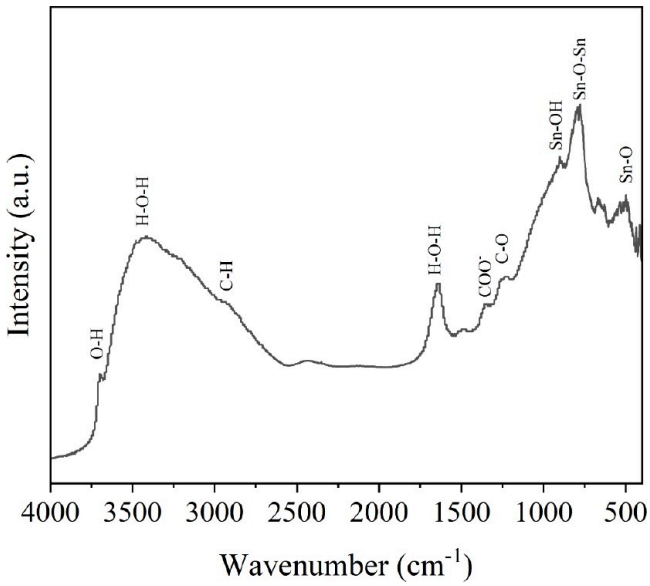


Figure 2. DRIFT spectrum of the resin-derived SnO_2 nanopowder.

The IR diffuse reflectance spectrum shows a broad band at approximately 3400 cm^{-1} assigned to O−H stretching vibrations of surface hydroxyl groups and adsorbed water, while the band at approximately 1630 cm^{-1} corresponds to H−O−H bending. Weak absorptions around 2920 cm^{-1} are attributed to C−H stretching, indicating residual organic species from the synthesis. The band at approximately 1360 cm^{-1} is associated with COO^- stretching, and a signal in the approximately 1240 cm^{-1} region corresponds to C−O vibrations, suggesting adsorbed carbonate. In the low-wavenumber region, characteristic bands of Sn−O and Sn−O−Sn vibrations are observed at approximately 520 and 780 cm^{-1}, confirming formation of the Sn−O lattice. Because DRIFT is qualitative in the present analysis, the weak organic-related bands indicate detectable surface species but do not establish their amount or a minimum residual-organic content.

3.2. Paste Rheology

The rheological properties of the SnO_2-loaded pastes were evaluated to assess their suitability for 3D printing by DIW, using SH94.4, a material with exemplary extrudable properties, as a benchmark. As shown in the flow curves in Figure 3A, all formulated pastes exhibited the essential pseudoplastic (shear-thinning) behavior required for extrusion, where viscosity decreases under increasing shear, enabling flow through a nozzle. This phenomenon is attributed to alignment of polymer binder chains and breakdown of particle agglomerates under stress.[12,22]

A detailed analysis of the rheological parameters, summarized in Figure 3B−D, reveals critical performance differences. While the SH94.4 benchmark possesses a modest apparent yield stress (31.1 Pa, Figure 3C), all SnO_2-loaded pastes offered a substantial increase. This is crucial for ensuring the shape fidelity of printed structures, as a sufficiently high yield stress allows filaments to support their own weight and the weight of subsequent layers.[23] However, an optimal rheological window exists, as an excessively high yield stress can prevent proper filament flow, leading to detrimental interfilament porosity in the final part.[13] The time-dependent response can be compared through the hysteresis-loop area (Figure 3D). RB-75.0 displayed a large positive area (11,907 Pa s^{-1}),

https://doi.org/10.1021/acsengineeringau.6c00022
ACS Eng. Au XXXX, XXX, XXX−XXX

Downloaded from pubs.acs.org/aeacb3/article-pdf/doi/10.1021/acsengineeringau.6c00022/6911515151/acsengineeringau.6c00022.pdf by CTR UNIV DA FEI user on 09 November 2026

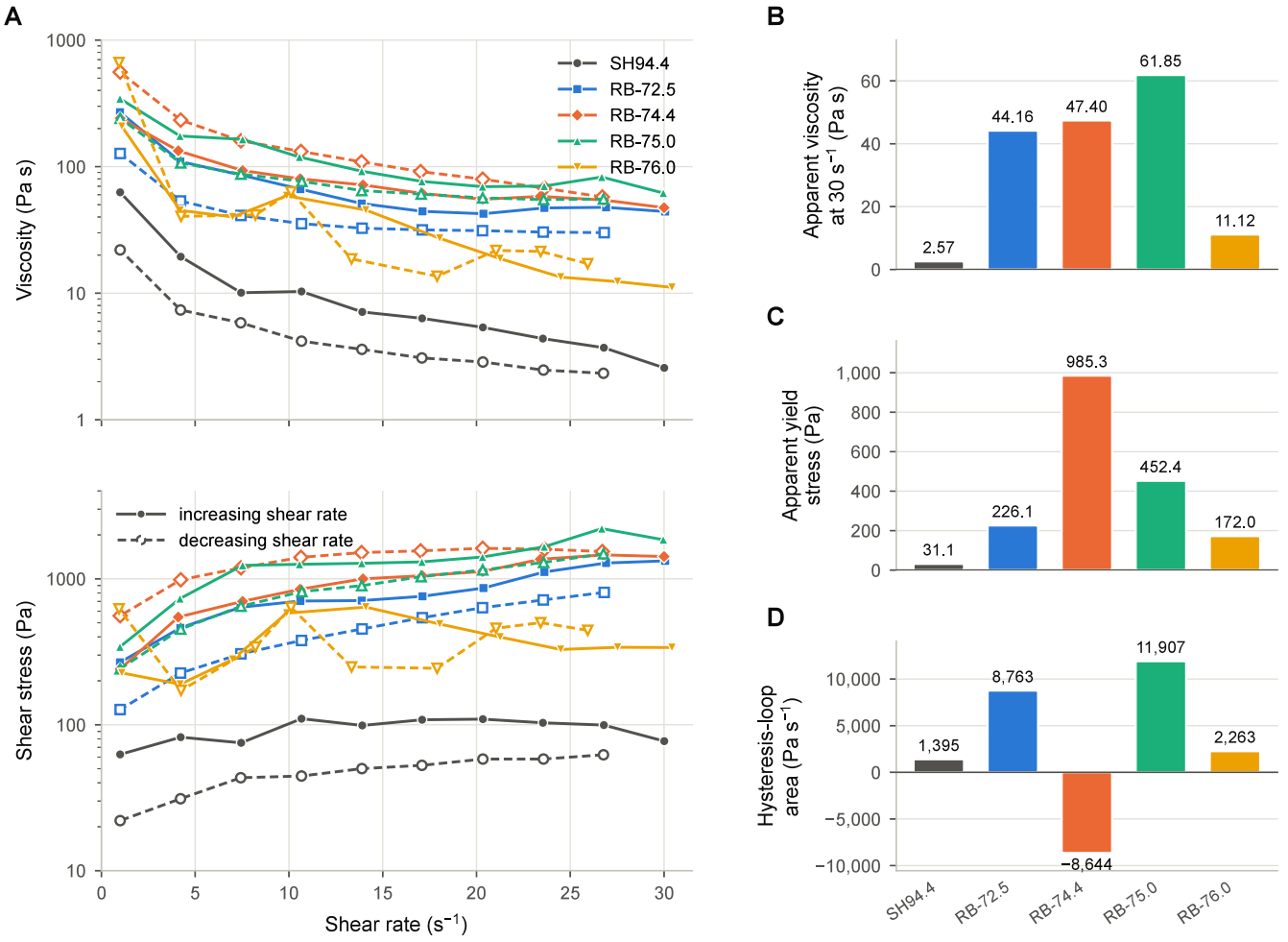


Figure 3. Rheological properties of the formulated ceramic pastes. (A) Full hysteresis loops for viscosity and shear stress plotted against shear rate; filled symbols with solid lines denote the increasing-rate branch, and open symbols with dashed lines the decreasing-rate branch. Each paste is shown in the same color in all panels. The derived quantitative parameters are summarized for (B) apparent viscosity at 30 s^{-1}, (C) operationally defined apparent yield stress, and (D) algebraic hysteresis-loop area calculated by the trapezoidal rule.

consistent with a clockwise loop and strong rebuilding over the specific test cycle.

In contrast, RB-74.4 exhibited a large negative hysteresis value (Figure 3D), corresponding to a counterclockwise loop. Hysteresis loops alone cannot be considered sufficient evidence of thixotropic or antithixotropic behavior because nonlinear viscoelastic effects may produce similar responses.[24] Counterclockwise loops may arise from either antithixotropy or nonlinear viscoelasticity, depending on the material and experimental conditions.[25] Therefore, the negative value observed here is interpreted as evidence of a distinct time-dependent structural evolution during the flow cycle rather than definitive proof of antithixotropic behavior. Such a response may affect postextrusion shape retention, but recovery kinetics were not measured independently in this study. These findings are consistent with meta-analyses of DIW ink design, which define a narrow rheological window where extrudability and shape fidelity coexist.[13] Barbosa et al.[12] further demonstrated that Pechini-derived polymeric binders can act dually as organic and inorganic binders, improving rheological control while contributing to oxide formation upon calcination. The present SnO_2 pastes extend this concept by showing that a reactive binder can improve viscoelastic properties while contributing the same target oxide to the calcined body.

3.3. Extrusion Evaluation

Following rheological characterization, the practical printability of each paste was evaluated using the DIW system with the 1.2 mm nozzle described in Section 2.3 and a maximum dispensing pressure of 3 bar. The test body was a thin-walled regular cylinder, as shown in Figure 4A. Extrusion trials were performed to validate the rheological predictions and identify a formulation capable of forming stable, self-supporting structures.

The initial screening revealed a critical processing challenge. RB-76.0 and RB-75.0 could not be extruded within the 3 bar pressure limit, consistent with their flow resistance. Conversely, RB-72.5 was easily extrudable; however, its apparent yield stress (226.1 Pa) was insufficient under the selected printing conditions, and the deposited lines were not self-standing, showing immediate slumping and collapse (Figure 4C). RB-74.4 could be extruded close to the equipment limit and was selected for printing. The comparison illustrates the narrow formulation window in which extrudability and shape retention coexist, as also reported for other ceramic DIW systems.[23]

RB-74.4 was successfully printed at approximately 2.9 bar, demonstrating smooth deposition and self-supporting behavior

Downloaded from pubs.acs.org/aeach3/article-pdf/doi/10.1021/acsengineeringau.6c00022/6911515/acsengineeringau.6c00022.pdf by CTR UNIV DA FEI user on 09 November 2026

https://doi.org/10.1021/acsengineeringau.6c00022
ACS Eng. Au XXXX, XXX, XXX−XXX

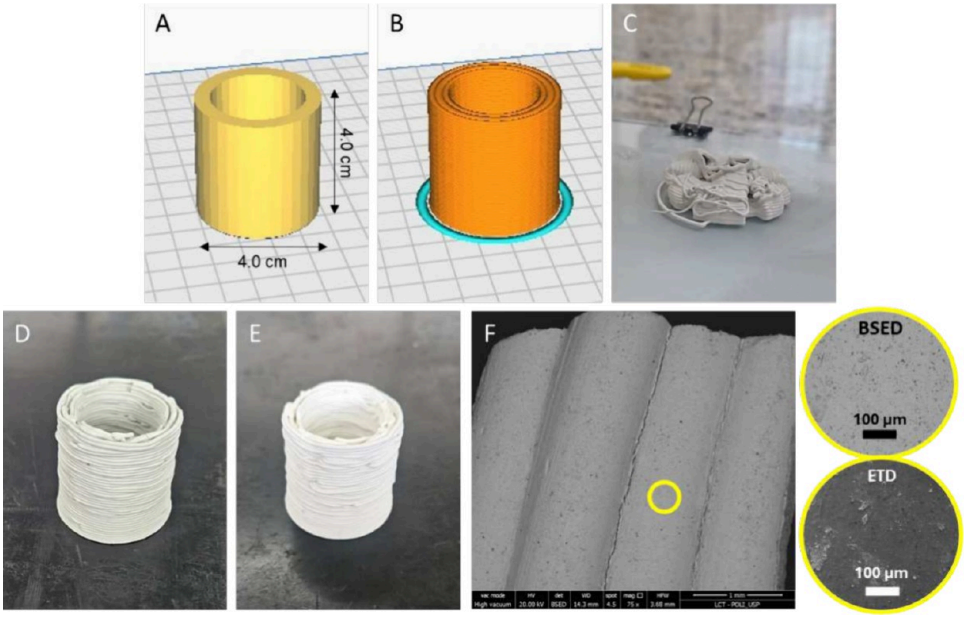


Figure 4. Direct ink writing of SnO_2 structures showing (A) the digital CAD model of the target geometry; (B) the sliced digital model illustrating the G-code toolpath; (C) structural collapse of the extruded RB-72.5 paste; (D) the self-supporting as-printed green body fabricated using RB-74.4; (E) the final SnO_2 ceramic cylinder after calcination; and (F) an SEM micrograph of the surface showing extruded filaments, together with higher-magnification views of the same region acquired using backscattered-electron and secondary-electron imaging modes.

during fabrication. A thin cylindrical green body was produced using this formulation, as shown in Figure 4D. Each formulation was prepared and evaluated as one batch; consequently, the marked change in printability between nearby solids loadings should be interpreted as evidence of a narrow process window rather than as a statistically established composition threshold.

Finally, the successfully printed green body was calcined. This thermal treatment removed the organic binder and promoted bonding between the SnO_2 particles, resulting in the self-supporting ceramic structure shown in Figure 4E. This demonstrates translation of a rheologically adjusted paste into a well-defined three-dimensional object. An enlarged view of the filaments is shown in Figure 4F, where junctions between adjacent filaments are visible, along with a fracture line in one filament. Higher-magnification BSE and SE views show an overall uniform topography. The terms "self-supporting" and "structural integrity" here describe visual retention of geometry and routine handling only; shrinkage, dimensional tolerances, strength, and fracture resistance were not quantified.

The successful printing of a structured SnO_2 piece represents an advance compared with approaches in which foreign binders may introduce additional inorganic species. Compared with Qi et al.,[26] who used digital light processing (DLP) printing of Sb-doped SnO_2 electrodes to improve conductivity, the present work targets a nominally undoped SnO_2 matrix and reactive-binder processing. Unlike starch-assisted or porogen-based strategies for hierarchical porosity,[27] the present approach establishes a baseline for subsequent incorporation of pore formers or mixed-oxide chemistries. The Si-rich inclusions discussed below show, however, that avoidance of foreign binder-derived cations does not by itself guarantee compositional control throughout processing.

The porosimetry results, detailed in Table 2, indicate a predominantly unimodal mercury intrusion distribution centered at approximately 100−150 nm, with a median intrusion diameter of 137.91 nm. The cumulative curve (Figure 5A) shows that most of the intruded volume is concentrated within this range. The maximum intrusion volume (0.1930 mL g^{-1}) and mercury-accessible porosity (54.8%) indicate a significant connected void fraction, while the total pore area (6.1070 m^2 g^{-1}) is moderate, consistent with the predominance of larger accessible pores or pore throats, which contribute more strongly to intrusion volume than to specific surface area. The data suggest that the accessible microstructure is dominated by interparticle voids formed during drying and calcination, with a limited contribution from accessible meso- or micropores.

Table 2. Parameters and Results of Mercury Intrusion Porosimetry Analysis of the Printed Material

Analysis parameter	Value	Result	Value
Hg density (g cm^{-3})	13.53	Maximum intrusion volume (mL g^{-1})	0.1930
Hg surface tension (N m^{-1})	0.485	Total pore area (m^2 g^{-1})	6.1070
Contact angle (deg)	130	Median intrusion diameter (nm)	137.91
Filling pressure (psi)	0.52	Mercury-accessible porosity (%)	54.8
Maximum pressure (psi)	59,945.06		
Equilibration time (s)	20		

Mercury intrusion porosimetry characterizes pores connected to the external surface through entrances accessible under the applied pressure and reports entrance or throat dimensions rather than a complete geometric description of each pore. It does not quantify closed porosity, and ink-bottle effects can cause large cavities to be represented by smaller constrictions. SEM therefore provides complementary direct observations of exposed surfaces and sectioned voids, consistent with the complementary use of bulk intrusion and

Downloaded from pubs.acs.org/aeach3/article-pdf/doi/10.1021/acsengineeringau.6c00022/6911515151/acsengineeringau.6c00022.pdf by CTR UNIV DA FEI user on 09 November 2026

https://doi.org/10.1021/acsengineeringau.6c00022
ACS Eng. Au XXXX, XXX, XXX−XXX

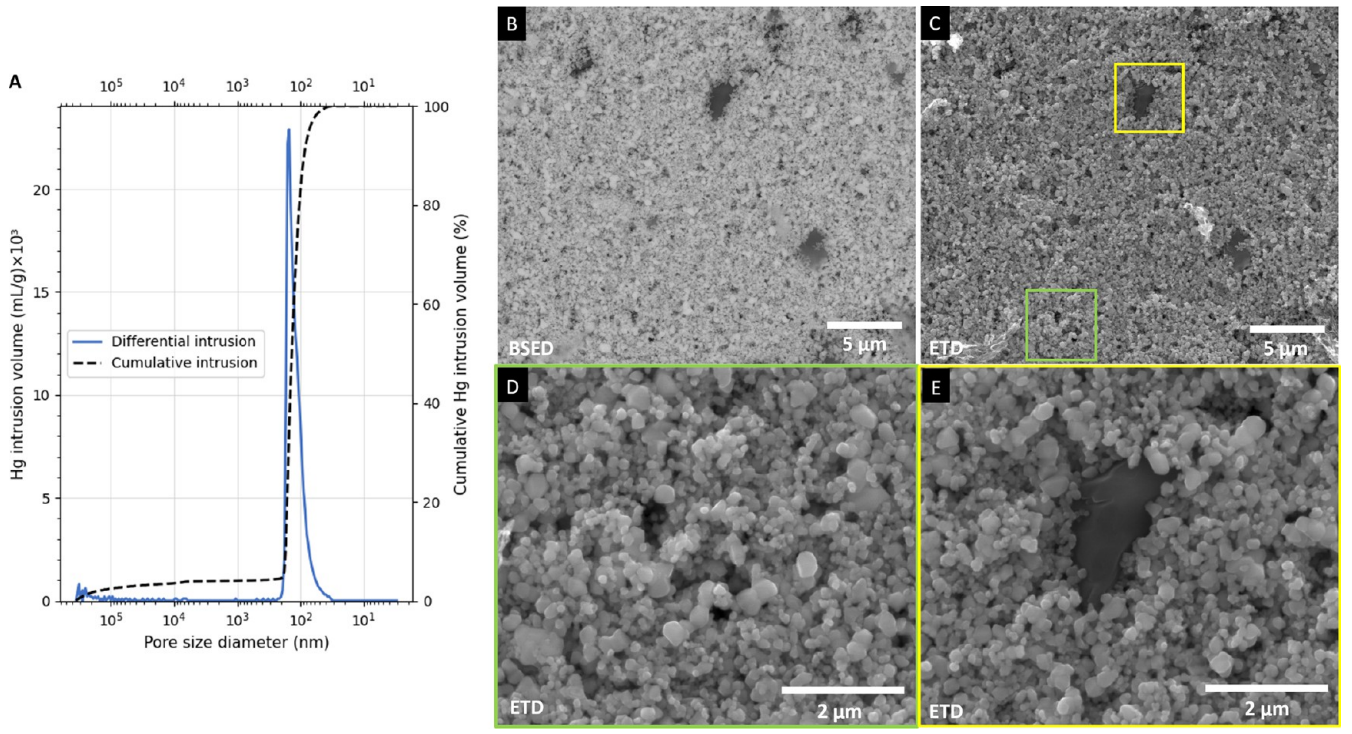


Figure 5. Porosity of the 3D-printed samples: (A) mercury intrusion curve and (B–E) surface inspection by SEM.

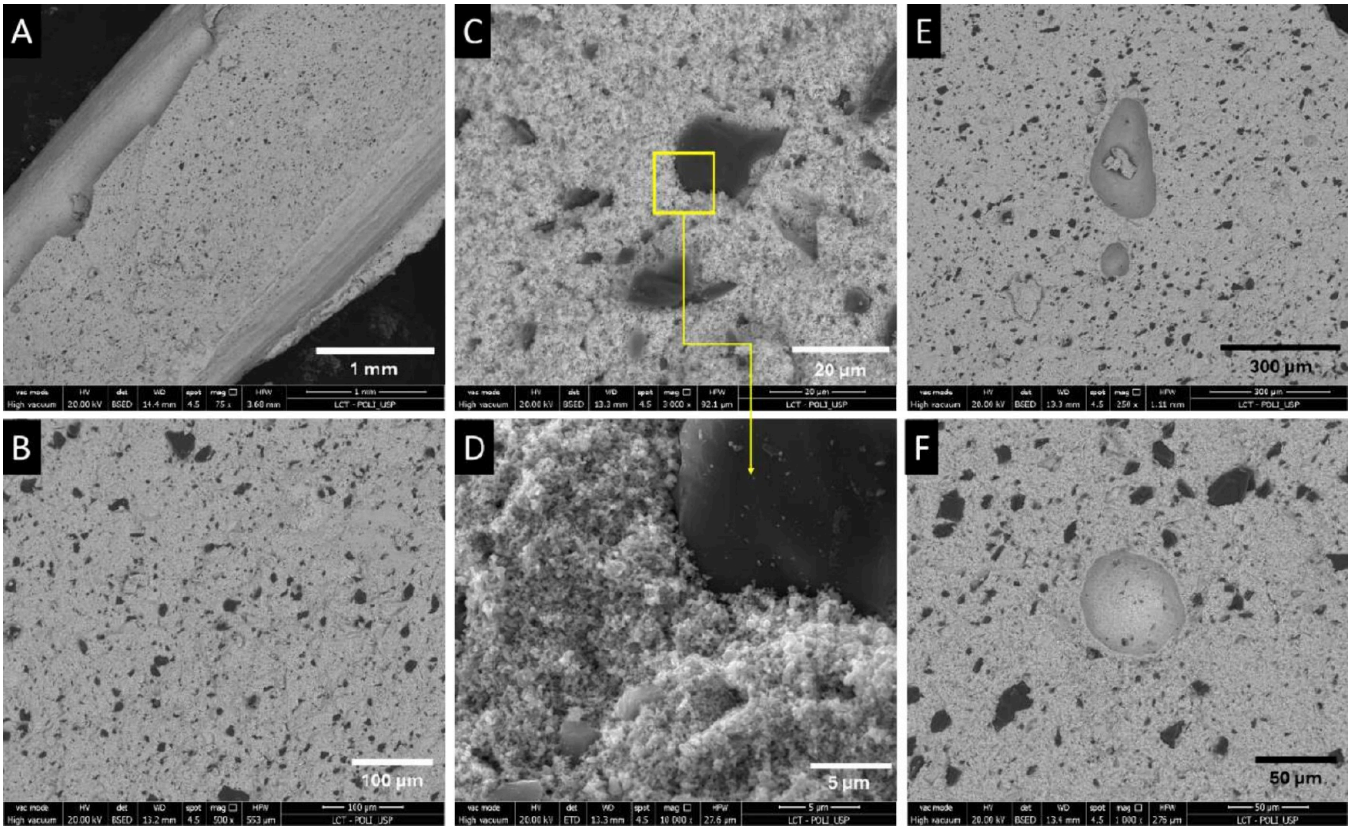


Figure 6. SEM micrographs of a fractured section of the sample, showing the increased presence of larger crystals and closed voids. Panel B is intentionally reused as panel D in Figure 7 for the quantitative comparison of surface and interior regions.

microscopy in studies of printed porous ceramics.[27,28] Although the total pore area obtained by intrusion (6.1 m^2 g^{-1}) is lower than the BET surface area of the synthesized powder (47.2 m^2 g^{-1}), the high mercury-accessible porosity indicates that the calcined matrix contains an interconnected network that can admit liquid precursors.

A visual inspection of the surface by SEM (Figure 5B–E) reveals micrometer-sized open features. Closer examination

https://doi.org/10.1021/acsengineeringau.6c00022
ACS Eng. Au XXXX, XXX, XXX–XXX

Downloaded from pubs.acs.org/aeach3/article-pdf/doi/10.1021/acsengineeringau.6c00022/6911515151/acsengineeringau.6c00022.pdf by CTR UNIV DA FEI user on 09 November 2026

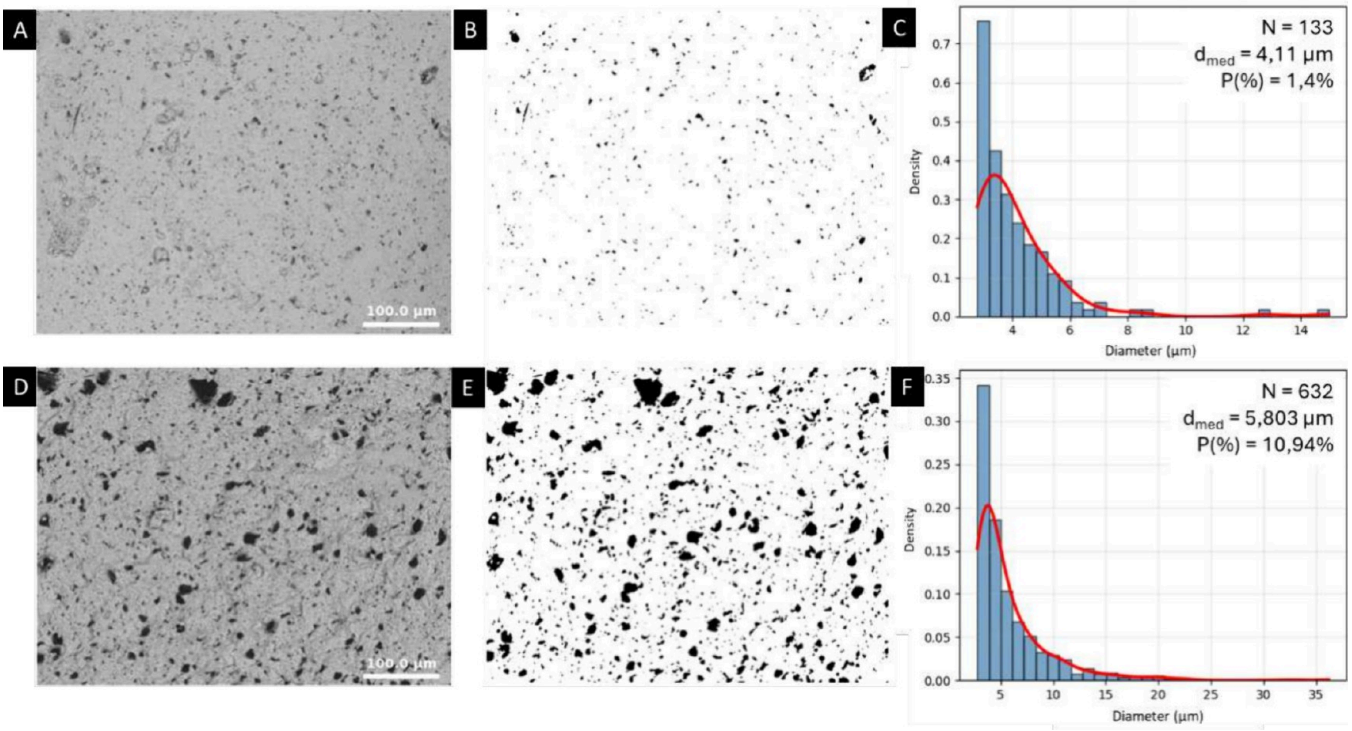


Figure 7. Distribution of heterogeneities at the surface (A–C) and in the interior (D–F) of the printed piece. Panel D intentionally repeats the fracture field in Figure 6B to connect the morphological and quantitative analyses.

(Figure 5E) shows that some apparent openings are instead associated with larger crystals embedded in the material. Their origin is examined by XRD, XRF, and EDS below.

Inspection of the fracture section shows a greater occurrence of these embedded crystals, as illustrated in Figure 6. In the inner volume of the piece, closed voids are also visible. These may have formed where local concentrations of Pechini resin released more gaseous products during calcination, although this proposed mechanism was not independently measured. The micrograph used in Figure 6B is intentionally shown again in Figure 7D because Figure 6 emphasizes fracture morphology and closed voids, whereas Figure 7 uses the same field as the basis for quantitative surface-to-interior comparison.

A comparative analysis of the heterogeneity observed in backscattered-electron images of the surface and interior (Figure 7) shows that foreign particles are more prevalent (approximately 5–10 times higher) in the interior of the piece (approximately 11% of the observed area) than at its surface (approximately 1.5% of the observed area). In addition, the average diameter of these heterogeneities is larger in the interior than at the surface, suggesting that some features observed at the surface correspond to corners of crystals embedded within the SnO_2 matrix. These observations show that the heterogeneities are physically embedded in the porous matrix. Preferential incorporation during mixing or redistribution during extrusion are possible explanations, but the present data do not distinguish between these mechanisms.

EDS analysis reveals that the compositional heterogeneity is associated with Si-rich inclusions in the printed body (Figure 8). XRD of the commercial SnO_2 powder showed only cassiterite (Figure 1B), while XRF quantified 0.07 wt % SiO_2 in the bulk starting powder (Table S1). The starting powder is therefore not completely Si-free, but its trace bulk Si level contrasts with the discrete micrometer-scale Si-rich inclusions observed by EDS. The localized morphology and greater occurrence of the inclusions within the printed body are most consistent with contamination introduced during paste production, probably as glass fragments from the beakers used in preparation. Consequently, the reactive binder avoids binder-derived foreign cations, but the printed supports cannot be described as compositionally controlled at the trace level. Establishing such control will additionally require eliminating contamination during paste preparation, for example by replacing glass vessels with polymer containers, and verifying the composition of the printed body itself rather than only that of the starting powders.

3.4. Catalyst Coating

To evaluate the viability of using the printed materials as catalyst supports, fragments of the printed sample were coated following the two procedures described previously, resulting in samples termed DD and ISS. Gravimetric analysis of the coated specimens is presented in Table 3. The average mass gains were similar within the observed dispersion: 7.82 ± 2.29 mg g^{-1} for DD and 8.63 ± 0.66 mg g^{-1} for ISS. The lower dispersion among the four ISS fragments suggests more reproducible mass uptake in this set, but gravimetry alone does not establish spatial uniformity; the distribution of Fe-containing material is assessed by imaging and EDS in Figures 9–13.

Figure 9 presents visual results for fragments prepared using the two coating methodologies. The material coated by direct deposition from an oxide suspension (Figure 9B) shows predominantly surface-level coverage with a high degree of heterogeneity, evidenced by variations in red color across the surface. In contrast, the material coated via in situ synthesis (Figure 9A) exhibits greater apparent penetration throughout the structure, visible as a color change in the inner core from white to brownish. Computational image analysis using the

https://doi.org/10.1021/acsengineeringau.6c00022
ACS Eng. Au XXXX, XXX, XXX–XXX

Downloaded from pubs.acs.org/aeacb3/article-pdf/doi/10.1021/acsengineeringau.6c00022/6911515151/acsengineeringau.6c00022.pdf by CTR UNIV DA FEI user on 09 November 2026

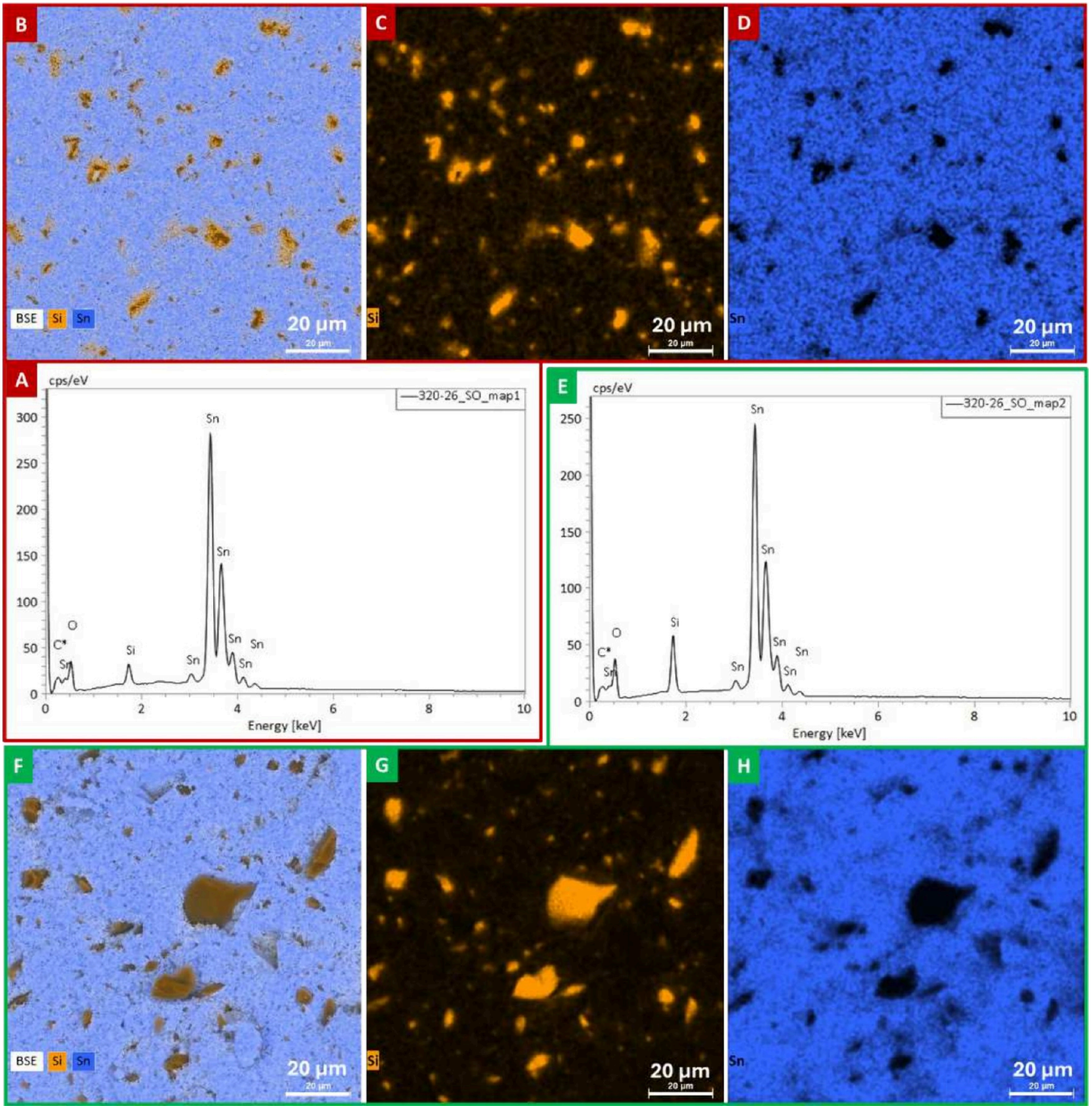


Figure 8. Energy-dispersive X-ray spectroscopy analysis of the interior of the printed material in two distinct regions (A–D and E–H): EDS spectra (A, E), composite elemental maps (B, F), and individual elemental maps for silicon (C, G) and tin (D, H).

Table 3. Gravimetric Analysis of the Coating Processes

Direct deposition			In situ synthesis		
Sample	Initial (g)	Final (g)	Sample	Initial (g)	Final (g)
DD1	0.2652	0.2676	ISS1	0.2834	0.2859
DD2	0.5593	0.5643	ISS2	0.3389	0.3419
DD3	1.1509	1.1612	ISS3	0.5735	0.5786
DD4	2.0444	2.0534	ISS4	2.0549	2.0706
Average mass gain ($mg\ g^{-1}$)		7.82 ± 2.29	Average mass gain ($mg\ g^{-1}$)		8.63 ± 0.66

saturation channel as an indicator of coating presence (Figure 9C) supports penetration into the internal structure. The ISS saturation profile nevertheless decreases toward the center of the fragment, so this optical analysis indicates penetration rather than uniform coverage. This qualitative result is consistent with infiltration through the accessible pore network; elemental evidence is presented below.

The coated samples do not exhibit major morphological differences compared with the uncoated specimen. Figure 10 shows representative internal features of an ISS sample. The fracture region reveals internal porosity and contrast variations in the backscattered-electron image. Higher-magnification polished cross-sections further show finely agglomerated material around pores, which is consistent with oxidation of

https://doi.org/10.1021/acsengineeringau.6c00022
ACS Eng. Au XXXX, XXX, XXX−XXX

Downloaded from pubs.acs.org/aeacb3/article-pdf/doi/10.1021/acsengineeringau.6c00022/6911515151/acsengineeringau.6c00022.pdf by CTR UNIV DA FEI user on 09 November 2026

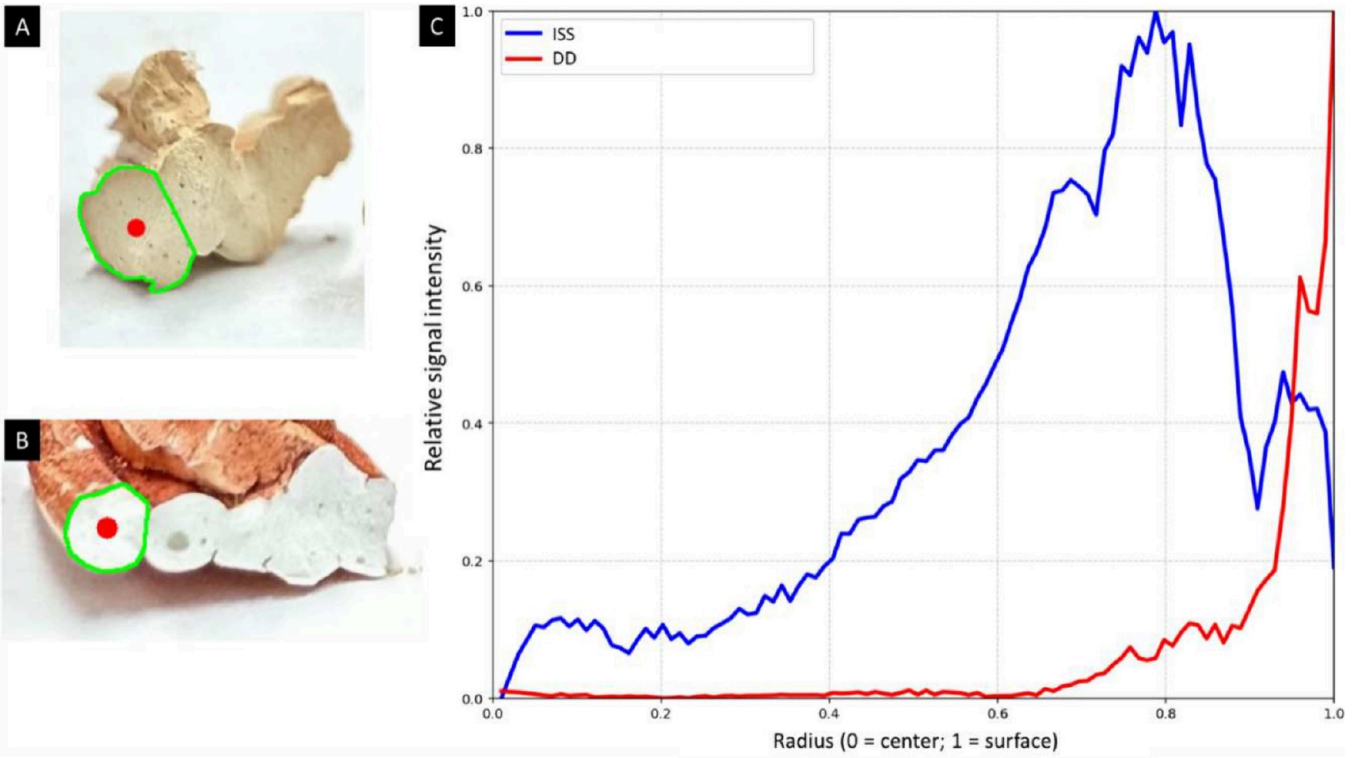


Figure 9. Visual inspection of fragments of SnO_2 specimens coated with Fe-containing species: (A) specimen coated by in situ synthesis (ISS); (B) specimen coated by deposition from suspension (DD); and (C) computational analysis of the extent of penetration of the coating material within the structure.

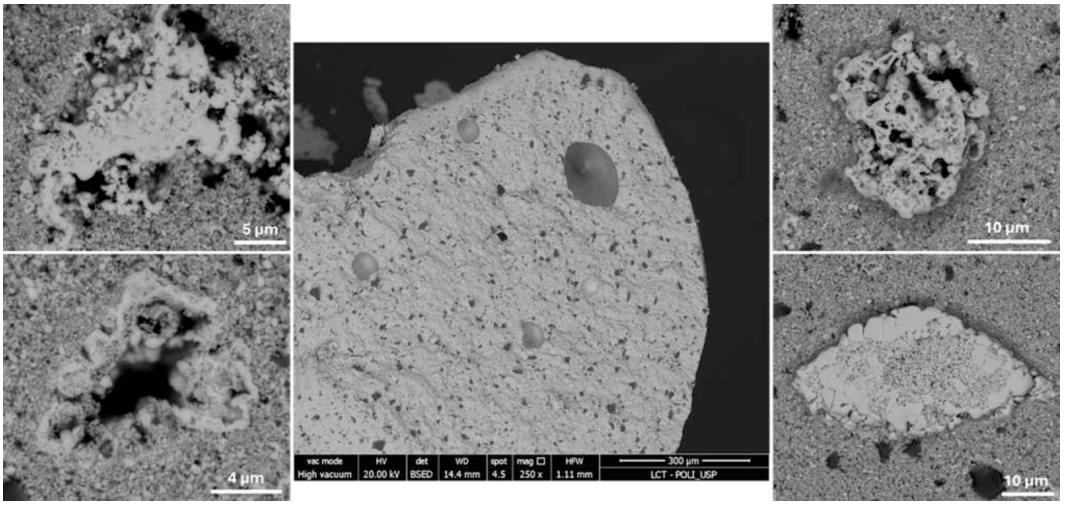


Figure 10. Representative micrographs of the sample coated by in situ synthesis.

the reactive-binder organic phase and simultaneous formation and local sintering of SnO_2. Backscattered-electron contrast alone, however, does not identify the Fe-containing phase or its oxidation state.

Regarding incorporation of Fe-containing species, EDS analysis corroborates the visual observations in Figure 9. Figure 11 shows an Fe signal on the surface, along fracture regions (Figure 11A–F) and in the cross-sectional analysis (Figure 11I–K). A line scan of the Fe Kα signal from the surface toward the center of a sectioned filament (Figure 11G,H) shows that the signal persists over the approximately 1 mm analyzed distance, with only a gradual decrease. Fitting a single exponential function, $I(x) = I_0 \exp(bx)$, to the data points gives a slight exponential decay constant b of −0.000257 μm^{-1}, corresponding to a fitted half-decay distance, ln 2/|b|, of approximately 2.7 mm. This analysis has several limitations. First, the exponential function is used only as an empirical descriptor of the trend; it is not a transport model derived from the infiltration and calcination steps. Second, the line-scan intensities are normalized Fe Kα counts rather than calibrated concentrations, and they are influenced by local porosity, polished-surface topography, and matrix composition. The sharp minima in Figure 11H, many of which coincide with dark features in the BSE image (pores or Si-rich inclusions), contribute scatter that a single exponential does not describe. Third, the half-decay distance exceeds the scanned length and

https://doi.org/10.1021/acsengineeringau.6c00022
ACS Eng. Au XXXX, XXX, XXX−XXX

Downloaded from pubs.acs.org/aeach3/article-pdf/doi/10.1021/acsengineeringau.6c00022/6911515/acsengineeringau.6c00022.pdf by CTR UNIV DA FEI user on 09 November 2026

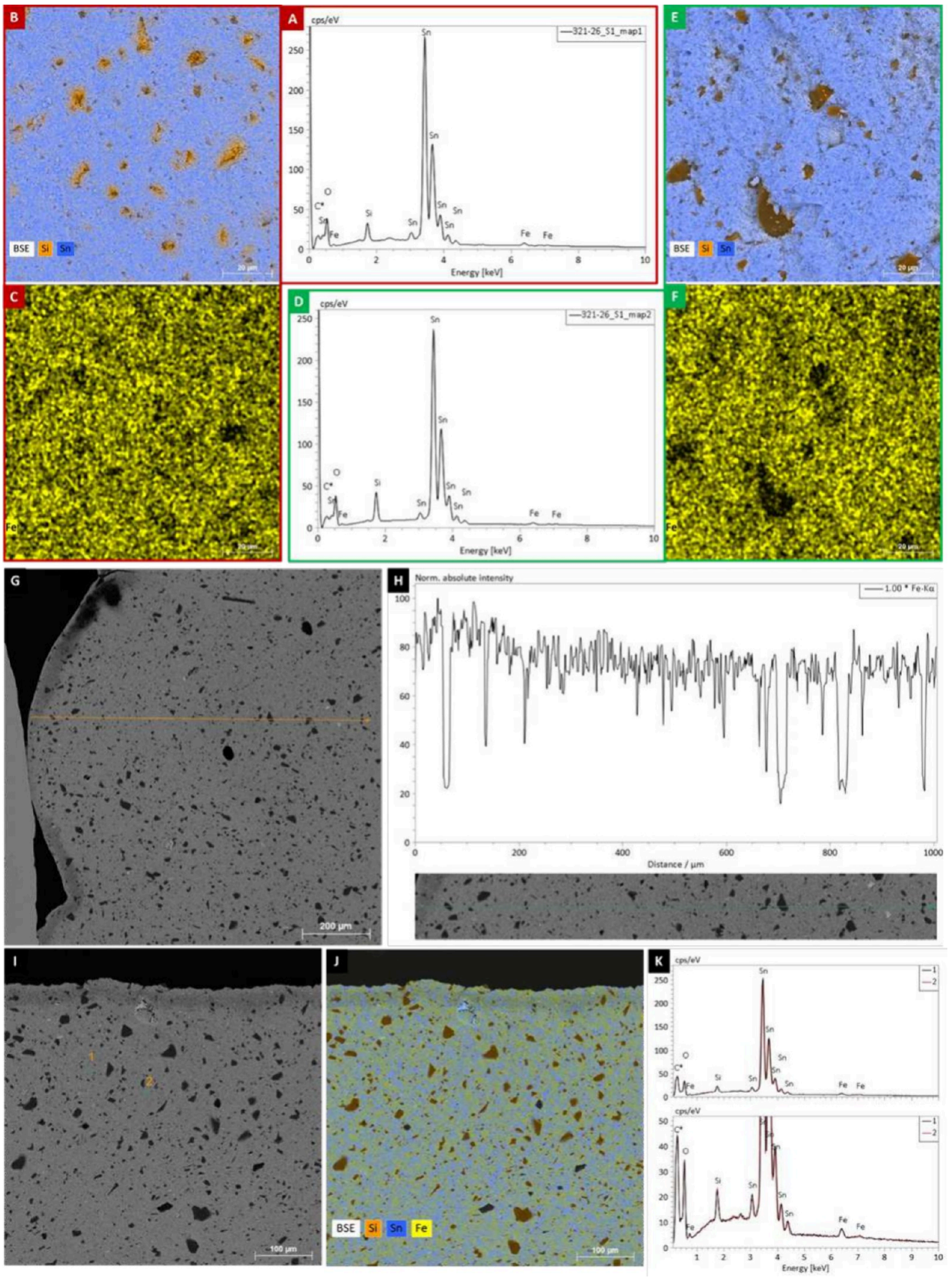


Figure 11. Elemental analysis of samples coated using the in situ synthesis method: representative EDS spectra (A, D), composite elemental maps (B, E, J), Fe elemental maps (C, F), line-scan analysis of Fe distribution across a filament cross-section (G, H), and cross-sectional micrographs with selected analysis points (I–K). The maps establish elemental Fe distribution in the analyzed regions but do not identify a crystalline Fe phase. The line scan in panel H is a single profile of normalized Fe Kα counts, not calibrated concentrations.

https://doi.org/10.1021/acsengineeringau.6c00022
ACS Eng. Au XXXX, XXX, XXX–XXX

Downloaded from pubs.acs.org/aeach3/article-pdf/doi/10.1021/acsengineeringau.6c00022/6911515151/acsengineeringau.6c00022.pdf by CTR UNIV DA FEI user on 09 November 2026

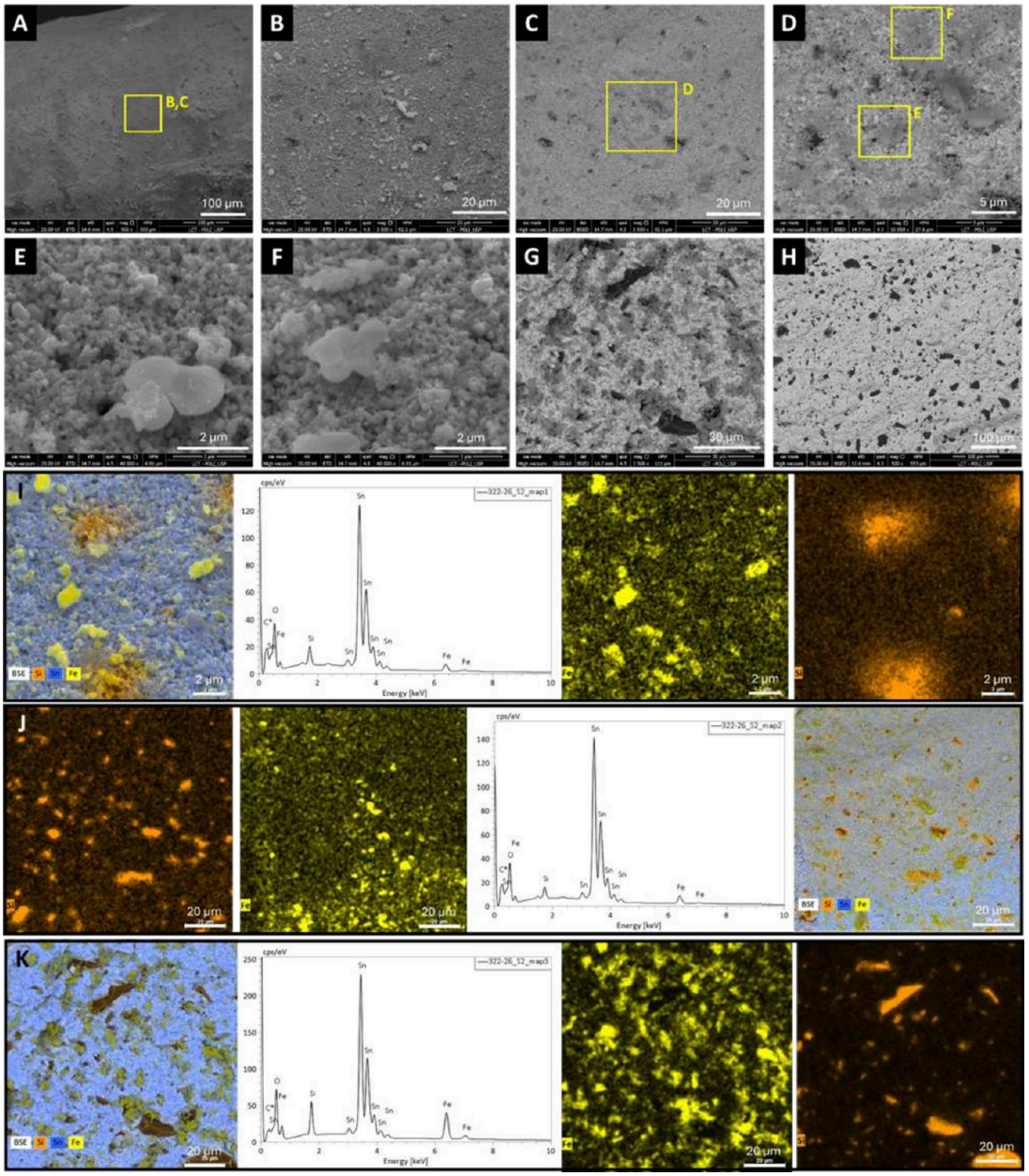


Figure 12. Microstructure of samples coated by the direct particulate deposition method: surface morphology at progressively higher magnifications (A–G) and a representative fracture region (H). Surface elemental analysis (I–K) reveals heterogeneously distributed Fe-rich agglomerates.

is therefore an extrapolation: it indicates that no strong attenuation was resolved over the analyzed distance, but it is not a measured penetration depth. Over the scanned distance itself, the fitted curve corresponds to a decrease of approximately 23%. Finally, the profile represents a single line in one cross-section. This analysis therefore supports volumetric incorporation within the examined filament rather than simple surface decoration, but it does not establish uniform Fe distribution throughout the entire printed structure. EDS confirms elemental Fe but cannot identify a crystalline phase or oxidation state.

Internal catalytic material can contribute only where reactants can access the connected pore network. Volumetric incorporation may increase the available coated region relative to surface-only deposition, but strong internal diffusion limitations could instead underutilize material in the filament interior. Transport and catalytic measurements are required to determine that balance. Fe is weak or absent in the Si-rich region along the line scan (Figure 11H), whereas similar Fe levels are observed at the two selected Sn-rich points (Figure 11I–K). This suggests that the Si-rich inclusions, probably glass-derived, may locally reduce uptake of the Fe-containing coating; the effect is spatially observed but was not quantified across replicate regions or batches.

In contrast, samples coated by direct deposition of particulate material exhibit a distinct surface morphology (Figure 12), characterized by Fe-rich agglomerates heterogeneously distributed over the surface. The increasing magnifications connect the macroscopic color heterogeneity with discrete surface deposits, and the EDS maps identify these deposits as Fe-rich regions.

https://doi.org/10.1021/acsengineeringau.6c00022
ACS Eng. Au XXXX, XXX, XXX–XXX

Downloaded from pubs.acs.org/aeach3/article-pdf/doi/10.1021/acsengineeringau.6c00022/6911515151/acsengineeringau.6c00022.pdf by CTR UNIV DA FEI user on 09 November 2026

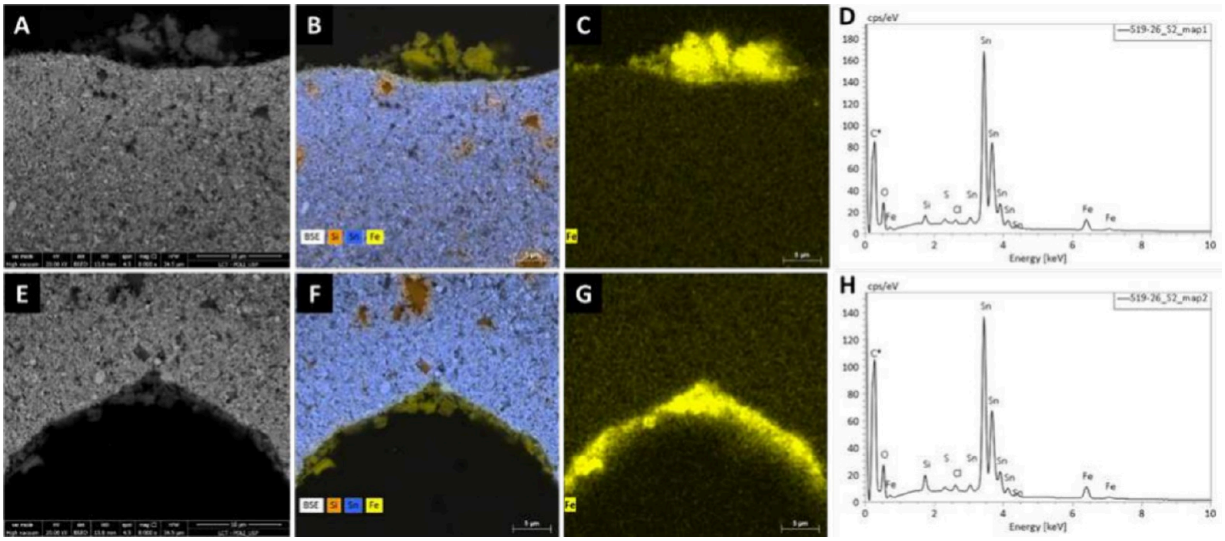


Figure 13. Polished cross-sectional micrographs of samples coated by the direct particulate deposition method: BSE images (A, E), composite elemental maps (B, F), Fe elemental maps (C, G), and corresponding EDS spectra acquired from the highlighted regions (D, H), showing Fe-rich surface agglomerates.

Analysis of a polished cross-section provides further evidence that the particles deposited by DD occur as randomly distributed agglomerates predominantly confined to the surface region (Figure 13). This is consistent with the mobility difference between a suspension of preformed particles and the lower-viscosity dissolved precursor used for ISS: the former is more readily retained at external pore entrances, whereas the diluted precursor resin can enter the connected pore network before calcination.

Together, the visual, cross-sectional, and EDS results show that ISS promotes penetration of Fe-containing species throughout the examined regions of the pore network, whereas DD leads predominantly to surface-localized agglomerates. These observations derive from a limited number of fragments, mapped fields, and a single line scan; demonstrating uniformity over the entire printed structure would require systematic EDS mapping at multiple positions along and across the printed body. The 1:4 dilution of the precursor resin lowers viscosity and favors entry into accessible pores or pore throats whose intrusion distribution is centered near 138 nm. The MIP result does not by itself prove transport through every pore or quantify closed porosity, but it is consistent with the observed infiltration.[29] The combination of similar average mass uptake and different spatial distributions further shows that deposition amount alone is not a proxy for volumetric uniformity.

4. CONCLUSION

In this work, we demonstrated a strategy for additive manufacturing of structured SnO_2 supports using DIW with a Pechini-derived reactive binder. The dual role of the binder, as both a rheological modifier and an in situ oxide precursor, enabled formulation of pastes with tailored viscoelastic properties while avoiding extraneous cations from an inorganic binder. Rheological analyses identified the balance between flow resistance and postdeposition shape retention required for printability, with RB-74.4 enabling extrusion close to the equipment pressure limit and retaining its geometry during layer-by-layer deposition. Because one batch of each formulation was examined, replicated processing studies are required to establish the reproducibility and width of this operating window.

The fabrication of a self-supporting SnO_2 piece after calcination demonstrates the potential of reactive-binder formulations to bridge the gap between laboratory-scale catalyst powders and structured supports. The terms self-supporting and structural integrity are limited here to visual shape retention and handling; mechanical strength, shrinkage, and dimensional fidelity remain to be quantified. The resin-derived SnO_2 had a BET surface area of 47.2 $m^2\ g^{-1}$, while MIP of the printed body indicated 54.8% mercury-accessible porosity and a median intrusion diameter of 137.91 nm.

Coating experiments further demonstrated the applicability of the printed structures as catalyst supports. While direct deposition produced heterogeneous, surface-localized Fe-rich agglomerates, the ISS route enabled comparatively homogeneous elemental Fe incorporation within the examined filament cross-sections. Because EDS mapping and the line scan sampled a limited number of regions, and the fitted half-decay distance is an extrapolation beyond the scanned length, uniform distribution throughout the entire printed structure was not established. In the absence of XRD data for a coated specimen, these deposits are conservatively designated Fe-containing species; EDS does not establish their crystalline phase or oxidation state. XRF quantified only 0.07 wt % SiO_2 in the as-received commercial SnO_2 powder; no XRF measurement was made on the paste or printed body. EDS nevertheless revealed discrete micrometer-scale Si-rich inclusions in the printed body. Trace Si from the powder cannot be excluded, but the inclusions most probably originated from glass fragments introduced from beakers during paste preparation.

Overall, the present strategy establishes a route for fabricating geometrically structured SnO_2 supports that are free of foreign binder-derived cations and suitable for infiltration-based incorporation of Fe-containing species. Full compositional control will additionally require eliminating processing contamination, such as the glass-derived Si-rich inclusions identified here, and verifying the composition of the

https://doi.org/10.1021/acsengineeringau.6c00022
ACS Eng. Au XXXX, XXX, XXX−XXX

Downloaded from pubs.acs.org/aeach3/article-pdf/doi/10.1021/acsengineeringau.6c00022/6911515151/acsengineeringau.6c00022.pdf by CTR UNIV DA FEI user on 09 November 2026

printed body. With these refinements, the approach could be extended to other metal-based catalysts.

■ ASSOCIATED CONTENT

Supporting Information

The Supporting Information is available free of charge at https://pubs.acs.org/doi/10.1021/acsengineeringau.6c00022.

Complete X-ray fluorescence composition of the as-received commercial SnO_2 powder (PDF)

■ AUTHOR INFORMATION

Corresponding Author

Bruno Ramos − *Microfluidic & Photoelectrocatalytic Engineering Lab, Department of Chemical Engineering, FEI University Center, São Bernardo do Campo, Brazil 09850-901; Laboratory of Ceramics Processes, Department of Metallurgical and Materials Engineering, Escola Politécnica, Universidade de São Paulo, São Paulo, Brazil 05508-900;* orcid.org/0000-0003-1932-6046; Email: brunoramos@fei.edu.br

Authors

Carolina Mendes Furlan Ferreira − *Microfluidic & Photoelectrocatalytic Engineering Lab, Department of Chemical Engineering, FEI University Center, São Bernardo do Campo, Brazil 09850-901*

Anderson Luis Barbosa − *Laboratory of Ceramics Processes, Department of Metallurgical and Materials Engineering, Escola Politécnica, Universidade de São Paulo, São Paulo, Brazil 05508-900;* orcid.org/0009-0000-8742-7362

Cátia Alexandra Podence Alves − *Laboratory of Ceramics Processes, Department of Metallurgical and Materials Engineering, Escola Politécnica, Universidade de São Paulo, São Paulo, Brazil 05508-900; LAQV-REQUIMTE, Department of Chemistry and Biochemistry, Faculty of Sciences, University of Porto, Porto, Portugal 4169-007;* orcid.org/0000-0002-7200-8154

Andre Luiz da Silva − *Laboratory of Ceramics Processes, Department of Metallurgical and Materials Engineering, Escola Politécnica, Universidade de São Paulo, São Paulo, Brazil 05508-900*

Douglas Gouvêa − *Laboratory of Ceramics Processes, Department of Metallurgical and Materials Engineering, Escola Politécnica, Universidade de São Paulo, São Paulo, Brazil 05508-900;* orcid.org/0000-0003-3607-8793

Complete contact information is available at: https://pubs.acs.org/10.1021/acsengineeringau.6c00022

Funding

The Article Processing Charge for the publication of this research was funded by the Coordenacao de Aperfeicoamento de Pessoal de Nivel Superior (CAPES), Brazil (ROR identifier: 00x0ma614).

Notes

The authors declare no competing financial interest.

■ ACKNOWLEDGMENTS

The authors acknowledge the support of the São Paulo Research Foundation (FAPESP), grants 23/14214-4 and 24/13525-9. We gratefully acknowledge the support of the RCGI—Research Centre for Greenhouse Gas Innovation (23.1.8493.1.9), hosted by the University of São Paulo (USP) and sponsored by FAPESP—São Paulo Research Foundation (2020/15230-5) and Shell Brasil, as well as the strategic importance of the support given by ANP (Brazil's National Oil, Natural Gas and Biofuels Agency) through the R&DI levy regulation.

■ REFERENCES

(1) Gothe, M. L.; Figueredo, A. L.; Borges, L. R.; Ramos, R.; Peixoto, A. F.; Vidinha, P. High-Pressure Hydrogenation: A Path to Efficient Methane Production from CO2. *Methane* **2024**, *3*, 53−64.

(2) Podence Alves, C. A.; Palharim, P. H.; Pratto, B.; Da Silva, A. L.; Gouvêa, D.; Ramos, B. Photocatalytic Ammonia Synthesis from Nitrogen in Water Using Iron Oxides: Comparative Efficiency of Goethite, Magnetite, and Hematite. *J. Photochem. Photobiol., A* **2025**, *460*, 116159.

(3) Palharim, P. H.; Gusmão, C.; Ramos, B.; Bento, R. T.; Pillis, M. F.; Teixeira, A. C. S. C. Highly Stable WO3-Ag-AgCl Films for Continuous Water Treatment Synthesized Using a New Low-Cost Ultrasonic Spray-Pyrolysis/Photoreduction Approach. *Journal of Environmental Chemical Engineering* **2024**, *12*, 112895.

(4) Fernandes, M. H.; Ramos, B.; Da Silva, A. L.; Gouvêa, D. Chloride-Doped ZnO Thin Films Prepared by Spray Pyrolysis: Effects on Microstructural, Optical, and Photocatalytic Properties. *Micro and Nanostructures* **2023**, *177*, 207550.

(5) Wu, C.-Y.; Lee, Y.-L.; Lo, Y.-S.; Lin, C.-J.; Wu, C.-H. Thickness-Dependent Photocatalytic Performance of Nanocrystalline TiO2 Thin Films Prepared by Sol-Gel Spin Coating. *Appl. Surf. Sci.* **2013**, *280*, 737−744.

(6) Ramos, B.; Couri, A. P.; Ookawara, S.; Costa Teixeira, A. C. S. Micro-Structured Packed Bed Reactors for Solar Photocatalysis: Impacts of Packing Size and Material on Light Harnessing. *Photochemical & Photobiological Sciences* **2019**, *18*, 577−582.

(7) An, K.; Alayoglu, S.; Musselwhite, N.; Plamthottam, S.; Melaet, G.; Lindeman, A. E.; Somorjai, G. A. Enhanced CO Oxidation Rates at the Interface of Mesoporous Oxides and Pt Nanoparticles. *J. Am. Chem. Soc.* **2013**, *135*, 16689−16696.

(8) Ivanova, S.; Pitchon, V.; Petit, C.; Caps, V. Support Effects in the Gold-Catalyzed Preferential Oxidation of CO. *ChemCatChem.* **2010**, *2*, 556−563.

(9) Wu, S.; Xu, X.; Zhang, X.; Ji, Z.; Jia, X.; Wang, X. 3D-Printing Functional Ceramic for One-Step Fabrication of Pd/C Catalytic Reactor. *Additive Manufacturing Frontiers* **2024**, *3*, 200167.

(10) Lewis, J. A. Binder Removal from Ceramics. *Annu. Rev. Mater. Sci.* **1997**, *27*, 147−173.

(11) Oropeza, D.; Hart, A. J. Reactive Binder Jet Additive Manufacturing for Microstructural Control and Dimensional Stability of Ceramic Materials. *Additive Manufacturing* **2021**, *48*, 102448.

(12) Barbosa, A. L.; De Oliveira Romano, R. C.; Bernardes, A. A.; Gouvêa, D. Rheological and Microstructural Characterization of Titania Pastes for Additive Manufacturing Using Polymeric Ceramic Precursor as Organic and Inorganic Binder. *Ceram. Int.* **2025**, *51*, 24072−24079.

(13) Li, Z. L.; Zhou, S.; Saiz, E.; Malik, R. Ink Formulation in Direct Ink Writing of Ceramics: A Meta-Analysis. *Journal of the European Ceramic Society* **2024**, *44*, 6777−6796.

(14) Inaba, M.; Murase, R.; Takeshita, T.; Yano, K.; Kosaka, S.; Takahashi, N.; Isomura, N.; Oh-ishi, K.; Yoshimune, W.; Tsuchiya, K.; Nobukawa, T.; Kodama, K. Synthesis of a Mesoporous SnO2 Catalyst Support and the Effect of Its Pore Size on the Performance of Polymer Electrolyte. *Fuel Cells. ACS Applied Materials & Interfaces* **2024**, *16*, 10295−10306.

(15) D'Arino, M.; Pinna, F.; Strukul, G. Nitrate and Nitrite Hydrogenation with Pd and Pt/SnO2 Catalysts: The Effect of the Support Porosity and the Role of Carbon Dioxide in the Control of Selectivity. *Applied Catalysis B: Environmental* **2004**, *53*, 161−168.

Downloaded from pubs.acs.org/aeach3/article-pdf/doi/10.1021/acsengineeringau.6c00022/6911515151/acsengineeringau.6c00022.pdf by CTR UNIV DA FEI user on 09 November 2026

(16) Anwar, M. Z.; Kim, D. J.; Kumar, A.; Patel, S. K. S.; Otari, S.; Mardina, P.; Jeong, J.-H.; Sohn, J.-H.; Kim, J. H.; Park, J. T.; Lee, J.-K. SnO2 Hollow Nanotubes: A Novel and Efficient Support Matrix for Enzyme Immobilization. *Sci. Rep.* **2017**, *7*, 15333.
(17) Tai, L.; Anderson, H. U.; Lessing, P. A. Mixed-Cation Oxide Powders via Resin Intermediates Derived from a Water-Soluble Polymer. *J. Am. Ceram. Soc.* **1992**, *75*, 3490−3494.
(18) Van Der Walt, S.; Schönberger, J. L.; Nunez-Iglesias, J.; Boulogne, F.; Warner, J. D.; Yager, N.; Gouillart, E.; Yu, T. Scikit-Image: Image Processing in Python. *PeerJ.* **2014**, *2*, e453.
(19) Kornilov, A.; Safonov, I.; Yakimchuk, I. A Review of Watershed Implementations for Segmentation of Volumetric Images. *Journal of Imaging* **2022**, *8*, 127.
(20) Sain, S.; Kar, A.; Patra, A.; Pradhan, S. K. Structural Interpretation of SnO2 Nanocrystals of Different Morphologies Synthesized by Microwave Irradiation and Hydrothermal Methods. *CrystEngComm* **2014**, *16*, 1079−1090.
(21) Medvedovski, E. Tin Oxide-Based Ceramics of High Density Obtained by Pressureless Sintering. *Ceram. Int.* **2017**, *43*, 8396−8405.
(22) del Mazo-Barbara, L.; Ginebra, M.-P. Rheological Characterisation of Ceramic Inks for 3D Direct Ink Writing: A Review. *Journal of the European Ceramic Society* **2021**, *41*, 18−33.
(23) Hossain, S. S.; Lu, K. Recent Progress of Alumina Ceramics by Direct Ink Writing: Ink Design, Printing and Post-Processing. *Ceram. Int.* **2023**, *49*, 10199−10212.
(24) Mewis, J.; Wagner, N. J. Thixotropy. *Adv. Colloid Interface Sci.* **2009**, *147−148*, 214−227.
(25) Wang, Y.; Ewoldt, R. H. Thixotropy, Antithixotropy, and Viscoelasticity in Hysteresis. *J. Rheol.* **2023**, *67*, 1199−1219.
(26) Qi, G.; Yao, H.; Zeng, Y.; Chen, J. Preparation and Properties of Highly Loaded SnO2-Based Porous Electrodes by DLP 3D Printing. *J. Alloys Compd.* **2023**, *935*, 167941.
(27) Tabard, L.; Garnier, V.; Prud'Homme, E.; Courtial, E.-J.; Meille, S.; Adrien, J.; Jorand, Y.; Gremillard, L. Robocasting of Highly Porous Ceramics Scaffolds with Hierarchized Porosity. *Additive Manufacturing* **2021**, *38*, 101776.
(28) Casas-Luna, M.; Torres-Rodríguez, J. A.; Valdés-Martínez, O. U.; Obradović, N.; Slámečka, K.; Maca, K.; Kaiser, J.; Montúfar, E. B.; Čelko, L. Robocasting of Controlled Porous CaSiO3-SiO2 Structures: Architecture-Strength Relationship and Material Catalytic Behavior. *Ceram. Int.* **2020**, *46*, 8853−8861.
(29) Niethammer, B.; Zormpa, F.; Hoang, G. T.; Slaby, N. A.; Zevaco, T. A.; Karakoulia, S.; Arnold, U.; Sauer, J. Conversion of Dimethyl Ether to Hydrocarbons Catalyzed by Pd-Loaded *MRE Zeolites. *Catal. Today* **2025**, *453*, 115258.

Downloaded from pubs.acs.org/aeacb3/article-pdf/doi/10.1021/acsengineeringau.6c00022/6911515151/acsengineeringau.6c00022.pdf by CTR UNIV DA FEI user on 09 November 2026

https://doi.org/10.1021/acsengineeringau.6c00022
ACS Eng. Au XXXX, XXX, XXX−XXX